nanomaterials

MDPI

Article

The Effect of Impact Load on the Atomistic Scale Fracture Behavior of Nanocrystalline bcc Iron

Zhifu Zhao [1,2,*], Zhen Wang [1], Yehui Bie [3], Xiaoming Liu [1,2] and Yueguang Wei [3]

[1] The State Key Laboratory of Nonlinear Mechanics (LNM), Institute of Mechanics, Chinese Academy of Sciences, Beijing 100190, China
[2] School of Engineering Science, University of Chinese Academy of Sciences, Beijing 100049, China
[3] Department of Mechanics and Engineering Science, College of Engineering, Peking University, Beijing 100871, China
* Correspondence: zhaozhifu@imech.ac.cn

Abstract: Nanocrystalline metals have many applications in nanodevices, especially nanoscale electronics in aerospace. Their ability to resist fracture under impact produced by environmental stress is the main concern of nanodevice design. By carrying out molecular dynamics simulations under different fast loading rates, this work examines the effect of impact load on the fracture behavior of nanocrystalline bcc iron at an atomistic scale. The results show that a crack propagates with intergranular decohesion in nanocrystalline iron. With the increase in impact load, intergranular decohesion weakens, and plastic behaviors are generated by grain boundary activities. Also, the mechanism dominating plastic deformation changes from the atomic slip at the crack tip to obvious grain boundary activities. The grain boundary activities produced by the increase in impact load lead to an increase in the threshold energy for crack cleavage and enhance nanocrystalline bcc iron resistance to fracture. Nanocrystalline bcc iron can keep a high fracture ductility under a large impact load.

Keywords: molecular dynamics simulation; nanocrystalline iron; impact load; fracture resistance; fracture ductility

check for updates

Citation: Zhao, Z.; Wang, Z.; Bie, Y.; Liu, X.; Wei, Y. The Effect of Impact Load on the Atomistic Scale Fracture Behavior of Nanocrystalline bcc Iron. *Nanomaterials* **2024**, *14*, 370. https://doi.org/10.3390/nano14040370

Academic Editor: Elisabetta Canetta

Received: 28 December 2023
Revised: 30 January 2024
Accepted: 5 February 2024
Published: 16 February 2024

Copyright: © 2024 by the authors. Licensee MDPI, Basel, Switzerland. This article is an open access article distributed under the terms and conditions of the Creative Commons Attribution (CC BY) license (https://creativecommons.org/licenses/by/4.0/).

1. Introduction

Nanocrystalline metals have many applications in nanodevices due to their good physicochemical properties [1–3]. Nanodevices, especially nanoscale electronics in aerospace, usually require high impact resistance. The ability of nanocrystalline metals to resist fracture under impact produced by environmental stress is the main concern of nanodevice design. Revealing the fracture behaviors and mechanisms of nanocrystalline materials is an important prerequisite for improving fracture resistance and evaluating service safety. Under an impact produced by environmental stress, nanodevices are subjected to stress with a large growth rate. The stress growth rate is determined by the magnitude of the impact load. The dependence of fracture behavior on stress growth rate is,, therefore, of great research interest. Experiments on polycrystalline metals have shown that the stress growth rate has significant effects on yield strength [4,5], tensile strength [5,6], fracture toughness [7–9], crack tunneling [10], and crack growth speed [11]. Different from polycrystalline metals, nanocrystalline metals have a large grain boundary proportion. The activities of grain boundaries and cracks and the interactions between them can seriously affect the fracture behavior of nanocrystalline metals. As a result, the fracture behavior of nanocrystalline metals under an impact produced by environmental stress may be significantly different from that of polycrystalline metals.

Atomic-scale techniques, such as in situ experiments and molecular dynamics simulations, can reveal the details of activities of grain boundaries and cracks and the interactions between them during nanocrystalline metal fractures. In situ experiments usually require

high-level operations for researchers, and the observed samples generally have defects and impurities [12]. Compared with in situ experiments, molecular dynamics simulations are more accessible and efficient. By carrying out molecular dynamic simulations on nanocrystalline metals without pre-existing cracks, researchers observed grain boundary migration as well as diffusion and dislocation nucleation and motion during nanocrystalline metal fractures [13–17]. For nanocrystalline metals with larger grain sizes, dislocation nucleation and motion are more obvious than grain boundary migration and diffusion [17–19]. The deformation of nanocrystalline metals is dominated by dislocation activities. With a decrease in grain size, a change in the dominant deformation mechanism from dislocation nucleation and motion-to-grain boundary migration and diffusion appears [17,18,20–23]. This change also results in the transition of the relationship between tensile strength and grain size from Hall–Petch to inverse Hall–Petch. Simulations showed that grain boundary mobility can be reduced by adding alloy atoms to improve the deformation behavior of nanocrystalline metals, such as doping Zr atoms at the grain boundaries in nanocrystalline Cu [24]. The activities of dislocation and grain boundaries can cause the breakage of atomic bonds and nanovoid nucleation at grain boundaries, particularly at the triple junctions [25–27]. The coalescence of nanovoids generates nanocracks. Nanocracks propagate along grain boundaries, which causes intergranular fractures [27–29]. Nanocrack initiation and propagation were observed to preferably take place at the high-angle grain boundaries perpendicular to the stretching direction [29]. Different from the fracture behavior of nanocrystalline metals without pre-existing cracks, dislocation and twinning are generated around crack tips besides grain boundary activities during the fracture of nanocrystalline metals with pre-existing cracks [30–34]. With crack propagation in nanocrystalline metals, nanovoids are usually generated at grain boundaries ahead of the crack [33]. A further study by the authors showed that these nanovoids are generated by intergranular decohesion that results from the fast Intergranular crack propagation on some cross-sections, and the fracture behavior of cracked nanocrystalline metals is dominated by crack propagation instead of grain boundary activities [34]. However, the high grain boundary proportion can indeed significantly improve the fracture toughness of nanocrystalline metals [32–34]. This improvement was found to be attributed to the weakening of intergranular decohesion [34].

As mentioned above, researchers obtained some valuable results regarding the fracture behavior of nanocrystalline metals by focusing on the activities of grain boundaries and cracks and the interaction between them. However, the competition between crack propagation and grain boundary activities under an impact environment remains unclear. Due to the requirements to achieve high saturation magnetic flux density with low losses and respond quickly to changes in external magnetic fields of the nanoscale electronics in aerospace, nanocrystalline bcc iron and its alloys with excellent soft magnetic properties have been developed and widely used [35–37]. The fracture failure of nanocrystalline iron has a significant effect on the reliability of nanoscale electronics. Hence, the authors of this work develop a large nanocrystalline bcc iron model with a pre-existing crack and investigate its fracture behavior under stretch loads with different fast growth rates by carrying out molecular dynamics simulations. The competition between crack propagation and grain boundary activities under impacts produced by environmental stress is fully discussed. It is believed that a better understanding of the nature of the large loading rate effect on nanocrystalline iron can be useful in preventing catastrophic failures of nanoscale electronics in aerospace when encourterning impacts produced by environmental stress.

2. Model and Methods

In this work, a nanocrystalline bcc iron model with average grain diameter of 15 nm was developed by Voronoi method, where the crystal orientation of each grain is random, as shown in Figure 1a. The Voronoi method was shown to produce nanocrystals with grain boundary structures similar to what is expected in polycrystalline material and log-normal grain size distributions similar to what is found in experiments [14,31] and is, therefore, widely used to construct the atomistic models [14–20,23–28,30–32,34]. The developed

model has $L_X \times L_Y \times L_Z$ dimensional size of 60 nm × 60 nm × 30 nm and 9,197,099 iron atoms. It is very isotropic and has a good inverse Hall–Petch relationship with nanocrystalline irons with average grain diameters of 5 nm and 10 nm [34]. After developing the nanocrystalline model, the processes of minimization, equilibration, and stretching simulation are performed in a large-scale atomic/molecular massively parallel simulator [38]. These processes are based on the precise description of the interactions between iron atoms. In this work, the embedded-atom potential developed by Mendelev et al. [39] is applied. During minimization, the conjugate gradient algorithm is used. The energy and force tolerances are 10^{-15}, and the maximum number of force and energy evaluations is 10^4. Due to the large dimensional size, minimization process is performed many times until the model state parameters remain unchanged. After minimization, an edge crack with front parallel to Z direction is created at the left of the model by directly deleting atoms, and its length in X direction is 20 nm. In Y direction, the crack is the same distance from the top and bottom of the model, as shown in Figure 1. Then, atomic initial velocities are set by a random number generator with the specified seed at the temperature of 1 K to avoid thermal effect. Based on atomic locations at the end of minimization and atomic initial velocities, the cracked model is fully equilibrated under microcanonical ensemble, where atomic velocities are explicitly rescaled to remain at a temperature of 1 K. After equilibration, the cracked model is stretched along Y direction by adding force on several layer atoms on the top and bottom under microcanonical ensemble, as shown in Figure 1a. In the directions of X and Y, free boundaries are applied to stretch the cracked model freely. In the directions of Z, periodic boundaries are applied to avoid the effect of extra surface on crack propagation. Additionally, the application of periodic boundaries puts the cracked model in a plane strain state. During the processes of equilibration and stretching simulation, velocity Verlet algorithm [40] is used to solve Newton's equations, and timestep is 10^{-3} ps. To identify the effect of loading rate on crack propagation in nanocrystalline bcc iron, the stretch process is performed five times, and the growth rates of stretch stress are 6.65 × 10^{-2} Gpa/ps, 1.33 × 10^{-1} Gpa/ps, 2.00 × 10^{-1} Gpa/ps, 2.66 × 10^{-1} Gpa/ps, and 3.33 × 10^{-1} Gpa/ps, respectively. As shown in Figure 1b–d, the distribution of grain boundaries and crystal orientation of grains are very different on different cross-sections normal to Z direction. Hence, the crack propagation behaviors on different cross-sections are very different. Discussion on the loading rate effect needs to consider crack propagation behaviors on different cross-sections.

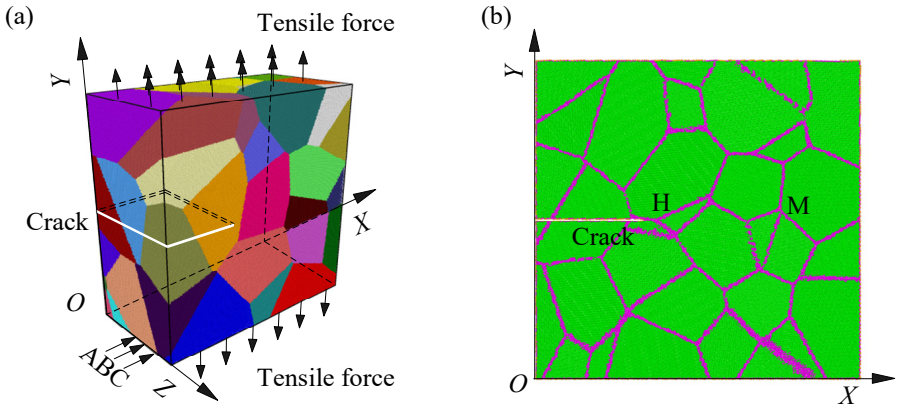


Figure 1. *Cont.*

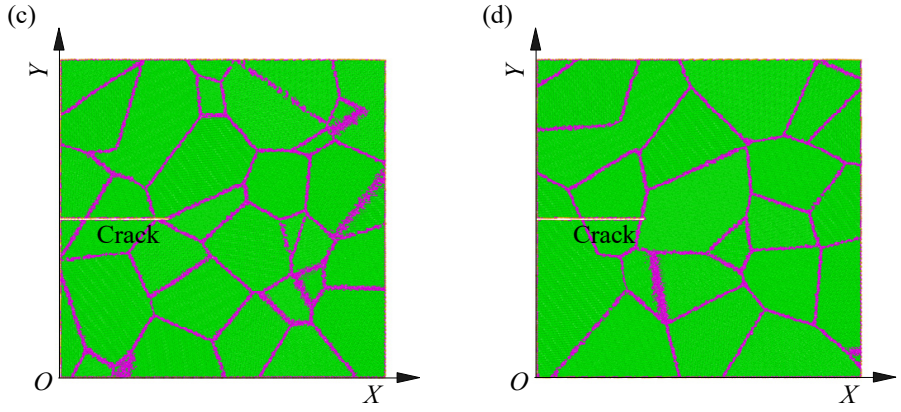


Figure 1. Nanocrystalline bcc iron model. (**a**) shows a 3D view, where colors are used to distinguish different grains. (**b**–**d**) show the distributions of grain boundaries and atoms on different cross-sections (A, B, and C) normal to *Z* direction, where the *Z* values of atoms on cross-section A are between 14.78 and 15.22 nm. Those on cross-section B are between 16.78 and 17.22 nm, and those on cross-section C are between 23.78 and 24.22 nm. In (**b**–**d**), green atoms have bcc crystal structure and are located inside the grains; pink ones are located at grain boundaries, and yellow ones are located at the surfaces of crack and model.

3. Results and Discussions

3.1. Engineering Stress–Strain Behaviors

Engineering stress–strain curve is a direct way to learn about the fracture behavior of nanocrystalline bcc iron. Under different loading rates, the engineering stress–strain behaviors of the cracked nanocrystalline bcc iron model varies greatly, as shown in Figure 2a. The ultimate tensile stress σ_b increases with the increase in loading rate in a weak nonlinear way. In other words, the second derivative of ultimate tensile stress with respect to loading rate is negative, which is consistent with the experimental results on steels without pre-existing cracks [41]. Plastic deformation becomes more significant with an increase in the loading rate. However, the shapes of stress–strain curves under loading rates lower than 2.00×10^{-1} GPa/ps are very different from those under loading rates higher than 2.00×10^{-1} GPa/ps. When the loading rate is lower than 2.00×10^{-1} GPa/ps, secondary hardening can be observed clearly. However, when the loading rate is higher than 2.00×10^{-1} GPa/ps, secondary hardening cannot be observed. Therefore, the mechanisms of plastic deformation under loading rates lower than 2.00×10^{-1} GPa/ps may be different from those under loading rates higher than 2.00×10^{-1} GPa/ps. The different plastic deformation mechanisms can lead to the obvious difference in fracture behavior of the cracked nanocrystalline model.

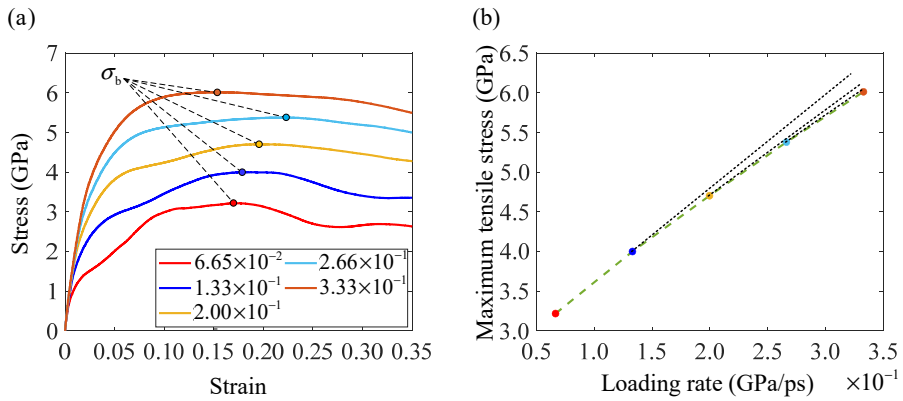
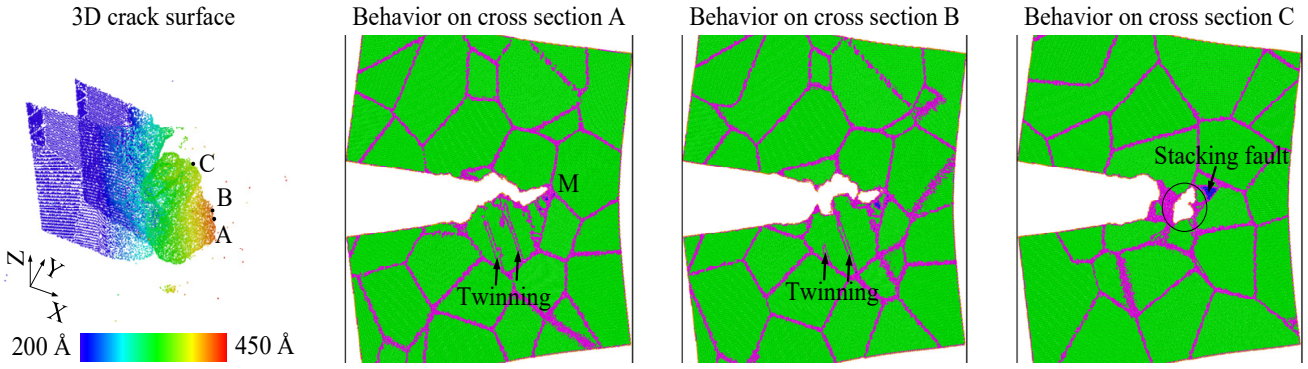


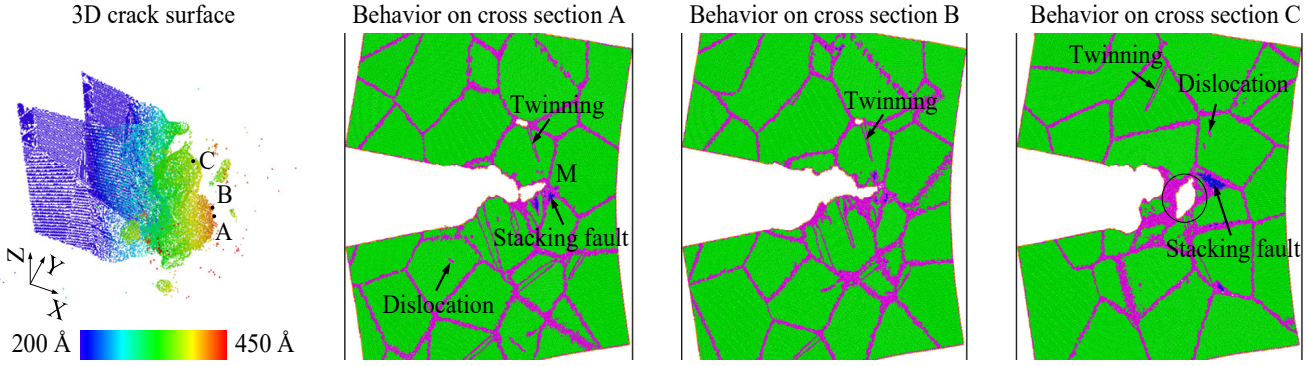
Figure 2. Engineering stress–strain behaviors under different loading rates, where (**a**) is the stress–strain curves and (**b**) is the maximum tensile stresses. The dashed lines in (**b**) are drawn linearly based on two adjacent points.

3.2. Crack Propagation Behaviors

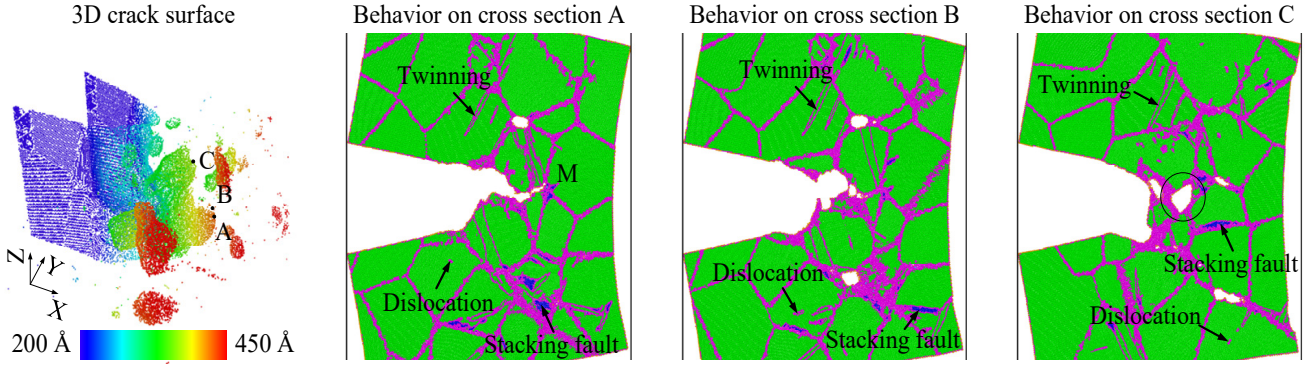
Figure 3 shows the crack propagation behaviors under different loading rates by visualization software OVITO (https://www.ovito.org/) developed by Stukowski [42], where the behaviors on different cross-sections are presented. During crack propagation, plastic behaviors, including stacking faults, twinning bands, and dislocations, can be generated. The common neighbor analysis [43], nearest neighbor number [44], centro-symmetry parameter [45], and atomic potential energy are calculated to identify the atoms correlated to plastic behaviors and differentiate them from surface atoms and bcc iron atoms. Details can be found in a previous study [34]. To examine the loading rate effect, the state of crack propagation when the crack tip first reaches the grain boundary junction of 'M' on section A is used as the criterion. Thus, the crack propagation behaviors in Figure 3a–c are at 40.4 ps, 23.8 ps, and 19.5 ps, respectively. As shown in Figure 3, brittle cleavage without obvious plastic deformation and ductile propagation with obvious plastic deformation can occur on different cross-sections. Fast brittle cleavage on some cross-sections can accelerate ductile propagation on their adjacent cross-sections through intergranular decohesion. For example, the void marked by a solid circle on cross-section C forms at grain boundaries and connects with the crack surface on cross-section A in Figure 3. The three-dimensional crack surface clearly describes the relationship between the marked void in section C and the crack tip in section A. From cross-section A to cross-section C, the void surface coincides with the grain boundaries, and the void size decreases gradually. Hence, the marked void is generated by the extension of fast cleavage on cross-section A along grain boundaries to cross-section C. This extension is a typical intergranular decohesion process. The marked void growth consumes the accumulated plastic deformation generated by crack transgranular propagation, and its convergence with the main crack can accelerate crack ductile propagation on cross-section C. With an increase in loading rate, the size of the void on cross-section C decreases, as well as the portion of the cross-section where fast cleavage occurs. As a consequence, the effect of intergranular decohesion weakens with the increasing loading rate. Additionally, one can find that more plastic behaviors are generated by grain boundary activities when the loading rate is increasing. The accumulation of this plastic deformation causes the formation of microvoids at the position far away from the crack tip. Because these microvoids are far away from the main crack, they cannot converge with the main crack. Plastic deformation and microvoid formation consume a lot of energy, so they seriously hinder the main crack propagation. The significant grain boundary activities are the main reasons for the weakening intergranular decohesion and high fracture toughness for a high loading rate. The fracture mechanism of nanocrystalline bcc iron is very different from that of coarse-grained iron under a high loading rate. Experimental results show that the fracture behavior of coarse-grained iron is determined by the twinning onset and dislocation motion at the crack tip under high loading rates [46]. There is no evidence that grain boundaries far from the crack tip provide sites for plastic deformation during the fracture process of coarse-grained iron specimens with a sharp crack. The high fracture toughness induced by obvious plastic deformation at grain boundaries in nanocrystalline bcc iron under high loading rates is instead similar to the fracture characteristics of metals or alloys with positive k_{ε_f} under quasi-static loading, where k_{ε_f} is an experimental constant indicating the relationship between fracture toughness and average grain size [47]. For metals or alloys with positive k_{ε_f}, grain refinement allows grain boundaries to offer sites for plastic deformation, which increases the energy expensed during ductile fracture and promotes fracture toughness. The differences in crack propagation behavior and grain boundary activity under different loading rates lead to differences in stress–strain behavior. When the loading rate is lower than 2.00×10^{-1} GPa/ps, crack propagation dominates the stress–strain behavior. The obvious ductile transgranular propagation can result in secondary hardening. When the loading rate is higher than 2.00×10^{-1} GPa/ps, grain boundary activities hinder crack propagation and dominate the stress–strain behavior. The fracture behavior of nanocrystalline bcc iron keeps high toughness due to the obvious grain boundary activities. Hence, secondary hardening cannot be observed.



(**a**) Crack propagation behavior under tensile stress with growth rate of 6.65×10^{-2} GPa/ps.



(**b**) Crack propagation behavior under tensile stress with growth rate of 2.00×10^{-1} GPa/ps.



(**c**) Crack propagation behavior under tensile stress with growth rate of 3.33×10^{-1} GPa/ps.

Figure 3. Crack propagation behaviors in nanocrystalline bcc iron under tensile stress with different growth rates, where cross-sections A, B, and C are atomic planes that contain points A, B, and C in 3D view, respectively. In the figure of 3D crack surface, the color gradient is on the basis of *X* coordinate value of iron atom. In the figures that depict behaviors on cross-sections A, B, and C, green and blue atoms have bcc and fcc crystal structures, respectively; pink ones are located at grain boundaries and dislocation cores, and yellow atoms are located at the surfaces of crack and voids.

3.3. Ductile–Brittle Characteristics

To further describe the effect of loading rate on the ductile–brittle characteristics of crack propagation, a quantitative investigation is carried out. The atoms with fcc, hcp, and ico crystal structures, and the atoms that are located at the dislocation cores and the boundaries of stacking faults and twinning bands, are defined as plastic atoms. The new surface atom number and the plastic atom number can be used to quantitatively describe crack propagation behavior. Figure 4 gives the new surface atom number and the plastic atom number at three random moments for each simulation. As shown in Figure 4, the difference between the new surface atom number at 40 ps and 35 ps is much larger than that between the new surface atom number at 35 ps and 30 ps for each simulation. Therefore, the

new surface atom number increases in a strong nonlinear way for each simulation; thus, its second derivative with respect to time is positive. The variation of the plastic atom number is similar to that of the new surface atom number. With an increasing loading rate, the new surface atom number and the plastic atom number also increase in a strong nonlinear way. However, their growth speeds have a significant difference. For example, the new surface atom number under the loading rate of 3.33×10^{-1} GPa/ps is 15.3 times that under the loading rate of 6.65×10^{-2} GPa/ps, while the plastic atom number under the loading rate of 3.33×10^{-1} GPa/ps is 30.74 times that under the loading rate of 6.65×10^{-2} GPa/ps. With an increase in loading rate, the plastic atom number grows faster than the new surface atom number.

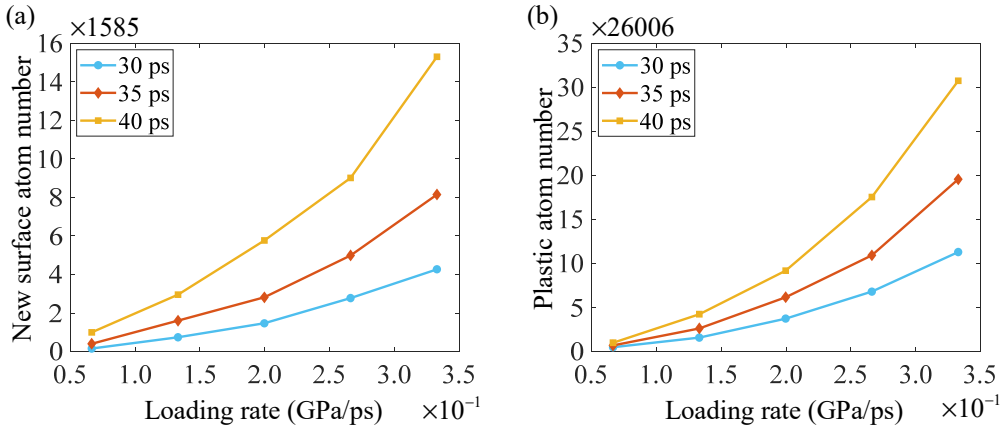


Figure 4. Variations of (**a**) new surface atom number and (**b**) plastic atom number during crack propagation under different loading rates.

According to fracture mechanics, the energy required to form a unit area of crack unilateral surface is usually used to measure the resistance to crack growth. For ductile fracture, the required energy contains the energy G_s consumed to form a crack surface and the energy G_p consumed to generate plastic deformation; thus

$$G_d = G_s + G_p \tag{1}$$

During new crack surface formation and plastic deformation generation, atomic kinetic and potential energies will increase. Compared with the increment of atomic potential energy, the increment of atomic kinetic energy is small and can be ignored. Hence, the increment of atomic potential energy is usually used to measure the resistance to crack growth [31]. Supplementary Figure S1 also shows that the change of atomic kinetic energy is related to the crack surface movement, but the change of atomic potential energy is related to the new crack surface formation and plastic deformation generation. Therefore, the calculations for G_s and G_p in this work only consider the increment of atomic potential energy. For the nanocrystalline model with a pre-existing crack, the value of G_p can be very large in the initial stage of crack cleavage because plastic behaviors can be generated before cleavage on most cross-sections. To avoid this situation, the term of G_p can be written as

$$G_p = \frac{\sum_{i=1}^{N_p} \Delta E_i^p}{A_0 + N_s/(2\rho_s)} \tag{2}$$

where N_p is the plastic atom number, ΔE_i^p is the extra potential energy that the ith atom gains when it participates in plastic deformation, A_0 is the initial area of crack unilateral surface, N_s is the new surface atom number, and ρ_s is the surface atom number on a unit

area. According to the pre-existing crack, the value of ρ_s is calculated as 10.173/nm^2. Similarly, the term of G_s can be computed as

$$G_s = \frac{\Gamma_0 + \sum_{j=1}^{N_s} \Delta E_j^s}{A_0 + N_s/(2\rho_s)} \quad (3)$$

where Γ_0 is the total potential energy of atoms on the initial surface of a pre-existing crack, and ΔE_j^s is the extra potential energy that the jth atom gains when it becomes a surface atom.

As shown in Figure 5, the energy required to form a unit area of crack unilateral surface increases with crack growth, which conforms to the ductile fracture characteristic of nanocrystalline bcc iron. When the crack starts to cleave, the threshold energy for crack cleavage increases with the loading rate increasing. However, no plastic behavior is generated at the same time in each simulation because the crack first cleaves in an intergranular way on some cross-sections, for example, cross-section A in Figure 1b. Before crack cleavage, the increasing number of atoms at grain boundaries is observed, and the decreasing number of atoms with bcc crystal structure is observed. With the increasing loading rate, the number of atoms at grain boundaries increases significantly before crack cleavage. Therefore, the increase in loading rate can promote the activity of grain boundaries in nanocrystalline bcc iron, which results in an increase in the threshold energy for crack cleavage and enhances the resistance to the fracture of nanocrystalline bcc iron. When the crack arrives at the grain boundary junction of 'H' on cross-section A, the intergranular crack propagation will be transformed into transgranular crack propagation at a small, limited distance. At the same time, cracks also propagate in a transgranular way on other cross-sections. Hence, the required energy G_d increases significantly with crack growth at this stage, as shown by the portion designated by PQ in Figure 5. When the loading rate is lower than 2.00×10^{-1} GPa/ps, crack propagation behavior is more obvious than grain boundary activities. The increase in loading rate can lead to an obvious increase in the growth rate of the required energy G_d. With the loading rate further increasing, grain boundary activities become more and more obvious. As a result, the growth rate of the required energy G_d cannot increase significantly, with the loading rate further increasing when the loading rate is more than 2.00×10^{-1} GPa/ps. Out of the stage designated by PQ, intergranular crack propagation occurs again on some cross-sections, and it will accelerate crack ductile growth on other cross-sections by intergranular decohesion. With the loading rate increasing, the intergranular decohesion weakens. The difference in the required energy G_d under different loading rates becomes obvious. When crack growth length is 250 Å, the required energy G_d under the loading rate of 3.33×10^{-1} GPa/ps is almost 2.62 times that under the loading rate of 6.65×10^{-2} GPa/ps and almost 4.7 times the Griffith energy release rate. In this work, the Griffith energy release rate is measured as 3.58 J/m^2. The fracture with high required energy G_d has a high ductility. The increase in loading rate can significantly increase the fracture ductility of nanocrystalline bcc iron.

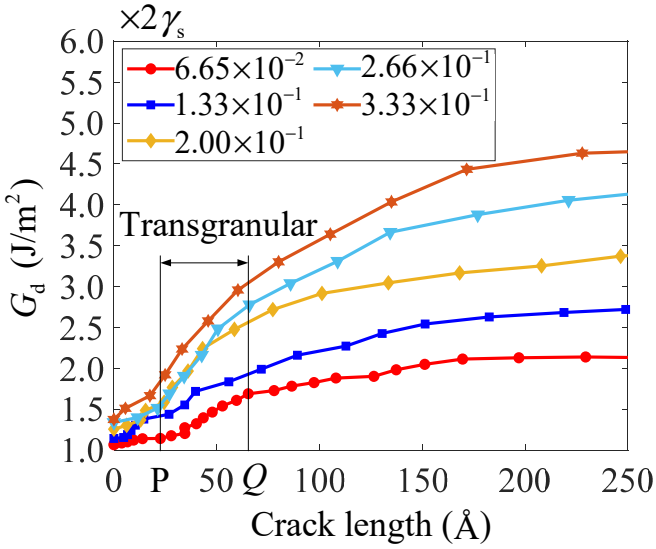


Figure 5. Variations of the energy required to form a unit area of crack unilateral surface with crack growth length under different loading rates.

4. Conclusions

This work investigates the atomistic scale fracture behaviors of cracked nanocrystalline bcc iron under different loading rates by carrying out molecular dynamics simulations. The main conclusions are as follows:

(1) The engineering stress–strain behaviors of cracked nanocrystalline iron are very disparate under different loading rates. On the one hand, the ultimate tensile stress increases with an increase in loading rate in a weak, nonlinear way. On the other hand, plastic deformation will cause secondary hardening of the stress–strain behavior at a low loading rate but not at a high loading rate.

(2) Ductile–brittle characteristics of crack propagation on different cross-sections are very unique, and fast brittle cleavage on some cross-sections can accelerate ductile propagation on their adjacent cross-sections through intergranular decohesion. With the loading rate increasing, intergranular decohesion weakens, and more plastic behaviors are generated by grain boundary activities. The obvious grain boundary activities result in the formation of microvoids at the position far away from the crack tip and hinder crack propagation. The differences in crack propagation behavior and grain boundary activity under different loading rates determine whether secondary hardening occurs or not.

(3) The promoted grain boundary activities by the increase in loading rate cause an increase in the threshold energy for crack cleavage and enhance the resistance to the fracture of nanocrystalline bcc iron. After crack cleavage, both the new surface atom number and the plastic atom number grow with an increase in loading rate in a strong, nonlinear way, but the plastic atom number grows faster than the new surface atom number. The increase in loading rate can significantly increase the fracture ductility of nanocrystalline bcc iron.

By applying stretch loads with different fast growth rates, this work provides a reference to reveal the fracture behaviors of nanocrystalline metals under different impact environments. The results have important implications for the safety design of related nanodevices.

Supplementary Materials: The following supporting information can be downloaded at: https://www.mdpi.com/article/10.3390/nano14040370/s1, Figure S1: The distributions of atomic kinetic and potential energies.

Author Contributions: Conceptualization, Z.Z.; methodology, Z.Z.; software, Z.Z.; validation, Z.Z., Z.W. and Y.B.; formal analysis, Z.Z.; investigation, Z.Z.; resources, Z.Z., X.L. and Y.W.; data curation, Z.Z.; writing—original draft preparation, Z.Z.; writing—review and editing, Z.Z.; visualization, Z.Z., Z.W. and Y.B.; supervision, Y.W.; project administration, Z.Z.; funding acquisition, Z.Z., X.L. and Y.W. All authors have read and agreed to the published version of the manuscript.

Funding: This research was funded by the National Natural Science Foundation of China (Grant Nos. 12202443, 12022210, 12032001).

Data Availability Statement: The data that support the findings of this study are available from the corresponding author upon reasonable request.

Acknowledgments: The authors acknowledge the anonymous referees for their helpful comments and constructive remarks on this manuscript.

Conflicts of Interest: The authors declare that they have no known competing financial interests or personal relationships that could have appeared to influence the work reported in this paper.

References

1. Chen, X.H.; Lu, J.; Lu, L.; Lu, K. Tensile properties of a nanocrystalline 316L austenitic stainless steel. *Scr. Mater.* **2005**, *52*, 1039–1044. [CrossRef]
2. Liu, J.C.; Zhou, X.L.; Zheng, X.; Cui, H.; Zhang, J.S. Tribological behavior of cold-sprayed nanocrystalline and conventional copper coatings. *Appl. Surf. Sci.* **2012**, *258*, 7490–7496. [CrossRef]
3. Azuma, D.; Ito, N.; Ohta, M. Recent progress in Fe-based amorphous and nanocrystalline soft magnetic materials. *J. Magn. Magn. Mater.* **2020**, *501*, 166373. [CrossRef]
4. Fan, C.Z.; Xu, Z.J.; Han, Y.; Liu, Y.; Huang, F.L. Loading rate effect and failure mechanisms of ultra-high-strength steel under mode II fracture. *Int. J. Impact Eng.* **2023**, *171*, 104374. [CrossRef]
5. Pandouria, A.K.; Yadav, K.; Tiwari, V. Compressive and tensile behavior of AA2014-T6 under different strain rates and different temperatures. *Structures* **2023**, *49*, 12–25. [CrossRef]
6. Wang, G.Z.; Ren, X.C.; Chen, J.H. Effects of loading rate on fracture behavior of low-alloy steel with different grain sizes. *Metall. Mater. Trans. A* **2004**, *35*, 1765–1778. [CrossRef]
7. Foster, J.T.; Chen, W.; Luk, V.K. Dynamic crack initiation toughness of 4340 steel at constant loading rates. *Eng. Fract. Mech.* **2011**, *78*, 1264–1276. [CrossRef]
8. Chaudhari, V.V.; Kulkarni, D.M. Influence of loading rate on fracture behaviour of extra deep drawn steel sheets. *Fatigue Fract. Eng. Mater. Struct.* **2015**, *38*, 851–859. [CrossRef]
9. Alfredsson, B.; Hazar, S.; Lai, J. Loading rate and temperature effects on the fracture toughness of a high strength bearing steel. *Eng. Fract. Mech.* **2021**, *245*, 107600. [CrossRef]
10. Xu, S.; Eagleson, R.; Tyson, W.R.; Park, D.Y. Crack tunnelling and crack tip opening angle in drop-weight tear test specimens. *Int. J. Fract.* **2011**, *172*, 105–112. [CrossRef]
11. Ambriško, Ľ.; Cehlár, M.; Marasová, D. The rate of stable crack growth (SCG) in automotive steels sheets. *Metalurgija* **2017**, *56*, 396–398.
12. Zeng, Y.H.; Chen, J.H.; Ma, X.Y.; Zeng, Z.D.; Yang, D.R. Grown-in defects in heavily phosphorus-doped Czochralski silicon. *Physica B* **2009**, *404*, 4619–4621. [CrossRef]
13. Swygenhoven, H.V.; Derlet, P.M.; Frøseth, A.G. Stacking fault energies and slip in nanocrystalline metals. *Nat. Mater.* **2004**, *3*, 399–403. [CrossRef] [PubMed]
14. Frederiksen, S.L.; Jacobsen, K.W.; Schiøtz, J. Simulations of intergranular fracture in nanocrystalline molybdenum. *Acta Mater.* **2004**, *52*, 5019–5029. [CrossRef]
15. Pan, Z.L.; Li, Y.L.; Wei, Q. Tensile properties of nanocrystalline tantalum from molecular dynamics simulations. *Acta Mater.* **2008**, *56*, 3470–3480. [CrossRef]
16. Zhang, L.; Shibuta, Y.; Huang, X.X.; Lu, C.; Liu, M. Grain boundary induced deformation mechanisms in nanocrystalline Al by molecular dynamics simulation: From interatomic potential perspective. *Comput. Mater. Sci.* **2019**, *156*, 421–433. [CrossRef]
17. Ma, K.; Sun, H.Y.; Qi, Y.; Ma, X. Grain size dependence of microstructure and mechanical properties of nanocrystalline TC4 alloy studied by molecular dynamic simulation. *Phys. Lett. A* **2023**, *481*, 129000. [CrossRef]
18. Tucker, G.J.; Tiwari, S.; Zimmerman, J.A.; McDowell, D.L. Investigating the deformation of nanocrystalline copper with microscale kinematic metrics and molecular dynamics. *J. Mech. Phys. Solids* **2012**, *60*, 471–486. [CrossRef]
19. Li, J.J.; Xian, Y.H.; Zhou, H.J.; Wu, R.N.; Hu, G.M.; Xia, R. Mechanical properties of nanocrystalline nanoporous gold complicated by variation of grain and ligament: A molecular dynamics simulation. *Sci. China-Technol. Sci.* **2018**, *61*, 1353–1363. [CrossRef]
20. Jeon, J.B.; Lee, B.J.; Chang, Y.W. Molecular dynamics simulation study of the effect of grain size on the deformation behavior of nanocrystalline body-centered cubic iron. *Scr. Mater.* **2011**, *64*, 494–497. [CrossRef]
21. Kumar, S.; Li, X.Y.; Haque, A.; Gao, H.J. Is stress concentration relevant for nanocrystalline metals? *Nano Lett.* **2011**, *11*, 2510–2516. [CrossRef]

22. Shimokawa, T.; Nakatani, A.; Kitagawa, H. Grain-size dependence of the relationship between intergranular and intragranular deformation of nanocrystalline Al by molecular dynamics simulations. *Phys. Rev. B* **2005**, *71*, 224110. [CrossRef]
23. Farkas, D.; Frøseth, A.; Swygenhoven, H.V. Grain boundary migration during room temperature deformation of nanocrystalline Ni. *Scr. Mater.* **2006**, *55*, 695–698. [CrossRef]
24. Wu, C.D.; Li, H.X. Molecular dynamics simulation of strengthening of nanocrystalline Cu alloyed with Zr. *Mater. Today Commun.* **2021**, *26*, 101963. [CrossRef]
25. Tang, Y.Z.; Bringa, E.M.; Meyers, M.A. Inverse Hall-Petch relationship in nanocrystalline tantalum. *Mater. Sci. Eng. A* **2013**, *580*, 414–426. [CrossRef]
26. Paul, S.K.; Kumar, S.; Tarafder, S. Effect of loading conditions on nucleation of nano void and failure of nanocrystalline aluminum: An atomistic investigation. *Eng. Fract. Mech.* **2017**, *176*, 257–262. [CrossRef]
27. Li, X.T.; Ma, W.T. Molecular dynamics simulation and theoretical modeling of free surface effect on nanocrack initiation induced by grain boundary sliding in nanocrystalline materials. *Mater. Lett.* **2021**, *304*, 130647. [CrossRef]
28. Cao, A.J.; Wei, Y.G. Atomistic simulations of crack nucleation and intergranular fracture in bulk nanocrystalline nickel. *Phys. Rev. B* **2007**, *76*, 024113. [CrossRef]
29. Bachurin, D.V. Influence of grain boundary misorientation on intergranular fracture of nanocrystalline palladium. *Int. J. Fract.* **2018**, *214*, 69–78. [CrossRef]
30. Pei, L.Q.; Lu, C.; Tieu, K.; Zhu, H.T.; Zhao, X.; Cheng, K.Y.; Zhang, L. A molecular dynamics simulation of fracture in nanocrystalline copper. *J. Nano Res.* **2013**, *23*, 50–56. [CrossRef]
31. Latapie, A.; Farkas, D. Molecular dynamics investigation of the fracture behavior of nanocrystalline α-Fe. *Phys. Rev. B* **2004**, *69*, 134110. [CrossRef]
32. Li, Q.H.; Dong, Z.B.; Zhou, S.Z.; Han, F.; Li, C.K.; Chang, H.; Zhang, Z.P. Investigation of grain boundary content on crack propagation behavior of nanocrystalline Al by molecular dynamics simulation. *Phys. Status Solidi B* **2022**, *259*, 2100570. [CrossRef]
33. Zhu, Y.H.; Hu, X.W.; Ni, Y.S. Molecular dynamics simulation of microstructure evolution during the fracture of nano-twinned Ag. *Eng. Fract. Mech.* **2021**, *248*, 107743. [CrossRef]
34. Zhao, Z.F.; Chu, F.L.; Wei, Y.G. Atomistic scale behaviors of crack propagation in nanocrystalline bcc iron. *Mater. Sci. Eng. A* **2021**, *809*, 140948. [CrossRef]
35. Qi, X.J.; You, J.H.; Zhou, J.F.; Qiu, K.Q.; Cui, X.L.; Tian, J.; Li, B.L. A review of fe-based amorphous and nanocrystalline alloys: Preparations, applications, and effects of alloying elements. *Phys. Status Solidi A* **2023**, *220*, 2300079. [CrossRef]
36. Chang, L.; Zhang, Y.Q.; Dong, Y.Q.; Li, Q.; He, A.N.; Chang, C.T.; Wang, X.M. Enhanced magnetic properties of Fe-based nanocrystalline composites by addition of carbonyl iron powders. *SN Appl. Sci.* **2019**, *1*, 902. [CrossRef]
37. Vetterick, G.; Baldwin, J.K.; Misra, A.; Taheri, M.L. Texture evolution in nanocrystalline iron films deposited using biased magnetron sputtering. *J. Appl. Phys.* **2014**, *116*, 233503. [CrossRef]
38. Plimpton, S. Fast parallel algorithms for short-range molecular dynamics. *J. Comput. Phys.* **1995**, *117*, 1–19. [CrossRef]
39. Mendelev, M.I.; Han, S.; Srolovitz, D.J.; Ackland, G.J.; Sun, D.Y.; Asta, M. Development of new interatomic potentials appropriate for crystalline and liquid iron. *Philos. Mag.* **2003**, *83*, 3977–3994. [CrossRef]
40. Swope, W.C.; Andersen, H.C.; Berens, P.H.; Wilson, K.R. A computer simulation method for the calculation of equilibrium constants for the formation of physical clusters of molecules: Application to small water clusters. *J. Chem. Phys.* **1982**, *76*, 637–649. [CrossRef]
41. Sun, X.; Soulami, A.; Choi, K.S.; Guzman, O.; Chen, W. Effects of sample geometry and loading rate on tensile ductility of TRIP800 steel. *Mater. Sci. Eng. A* **2012**, *541*, 1–7. [CrossRef]
42. Stukowski, A. Visualization and analysis of atomistic simulation data with OVITO—The Open Visualization Tool. *Model. Simul. Mater. Sci. Eng.* **2010**, *18*, 015012. [CrossRef]
43. Helio, T.; Paulo, S.B.; Jose, P.R. Structural characterization of deformed crystals by analysis of common atomic neighborhood. *Comput. Phys. Commun.* **2007**, *177*, 518–523.
44. Wolde, P.R.; Ruiz-Montero, M.J.; Frenkel, D. Numerical calculation of the rate of crystal nucleation in a Lennard-Jones system at moderate undercooling. *J. Chem. Phys.* **1996**, *104*, 9932. [CrossRef]
45. Kelchner, C.L.; Plimpton, S.J.; Hamilton, J.C. Dislocation nucleation and defect structure during surface indentation. *Phys. Rev. B* **1998**, *58*, 11085. [CrossRef]
46. Tanaka, M.; Wilkinson, A.J.; Roberts, S.G. Ductile–brittle transition of polycrystalline iron and iron–chromium alloys. *J. Nucl. Mater.* **2008**, *378*, 305–311. [CrossRef]
47. Fan, Z.Y. The grain size dependence of ductile fracture toughness of polycrystalline metals and alloys. *Mater. Sci. Eng. A* **1995**, *191*, 73–83. [CrossRef]

Disclaimer/Publisher's Note: The statements, opinions and data contained in all publications are solely those of the individual author(s) and contributor(s) and not of MDPI and/or the editor(s). MDPI and/or the editor(s) disclaim responsibility for any injury to people or property resulting from any ideas, methods, instructions or products referred to in the content.